processes

MDPI

Article

Comparative Study on Experiment and Numerical Simulation of Annular Multiphase Flow

Hongtao Jing [1,2,3,4], Wei Li [1,2,3,4], Chang'e Kong [1,2,3,4], Jianxin Shen [1,2,3,4], Qisong Lei [1,2,3,4], Bin Ma [5,6], Wei Luo [7,*] and Jihan Wang [7]

1 PetroChina Tarim Oilfield Company, Korla 841000, China; jinghongtao-tlm@petrochina.com.cn (H.J.); liwei5-tlm@petrochina.com.cn (W.L.); kce-tlm@petrochina.com.cn (C.K.); sjianxin-tlm@petrochina.com (J.S.); leiqs-tlm@petrochina.com.cn (Q.L.)
2 R&D Center for Ultra Deep Complex Reservoir Exploration and Development, China National Petroleum Corporation, Korla 841000, China
3 Engineering Research Center for Ultra-Deep Complex Reservoir Exploration and Development, Xinjiang Uygur Autonomous Region, Korla 841000, China
4 Xinjiang Key Laboratory of Ultra-Deep Oil and Gas, Korla 841000, China
5 Oil Production Technology Research Institute, PetroChina Tuha Oilfield Company, Hami 839009, China; mbwm@petrochina.com.cn
6 PetroChina Gas Lift Technology Center, Hami 839009, China
7 Petroleum Engineering Institute, Yangtze University, Wuhan 430100, China; wangjihan2002666@163.com
* Correspondence: luoruichang@163.com

Abstract

Annular gas–liquid flow is more complex than the flow in circular pipes because the inner and outer walls can support two liquid films. This study addresses the limited quantitative information available for inclined, dual-size annuli by combining controlled air–water experiments with three-dimensional transient computational fluid dynamics (CFD). Tests were conducted in a 5 m annular test section with a 38.5 mm tubing outer diameter and casing inner diameters of 75.9 and 62 mm at inclination angles of 45° and 90°. The experimental matrix covered air inlet velocities of 0.295–3.00 m/s and water inlet velocities of 0.20–2.00 m/s. Flow morphology was recorded by a high-speed camera, while pressure drop and liquid holdup were measured by differential pressure transducers and a conductivity probe, respectively. A transient volume-of-fluid (VOF) model coupled with the renormalization-group (RNG) k-ε turbulence model reproduced the same test section. The numerical and experimental flow morphologies agree for bubbly, slug, and annular flow. The predicted pressure drop follows the experimental trend with $R^2 = 0.92$ and an average absolute error of 7.91%, whereas the conventional Beggs-Brill, Mukherjee, Aziz, Hasan, and JPI correlations show larger average absolute errors. The principal advance of this work is a consistent experimental-numerical assessment of dual-film annular flow under two annulus sizes and two inclination angles, together with an explicit account of the remaining validation and measurement limitations. The results provide a basis for improving pressure-drop prediction in inclined coiled-tubing gas-lift wells.

Keywords: annular multiphase flow; flow pattern characteristics; numerical simulation; pressure-drop comparison

Check for updates

Academic Editor: Qingbang Meng

Received: 25 September 2025
Revised: 21 September 2026
Accepted: 13 October 2026
Published: 4 November 2026

Copyright: © 2026 by the authors. Licensee MDPI, Basel, Switzerland. This article is an open access article distributed under the terms and conditions of the Creative Commons Attribution (CC BY) license.

1. Introduction

1.1. Research Background

The available pressure in the Tarim Oilfield gas transmission network is limited. To use this gas as a high-pressure source for gas-lift dewatering and production, a combined

coiled-tubing and gas-lift-valve system is used. Gas is injected through the coiled tubing, and production occurs through the annulus between the coiled tubing and the production tubing. This configuration reduces the gas-lift startup pressure and increases the achievable dewatering depth. Current coiled-tubing gas-lift designs still rely on circular-pipe multiphase-flow models. However, the flow between the coiled tubing and production tubing is annular and is further complicated by the presence of inner and outer liquid films. Applying circular-pipe flow-pattern and pressure-drop correlations directly to the annulus can therefore cause significant errors. Detailed research on annular multiphase flow is consequently required to support coiled-tubing gas-lift design.

1.2. Research Status

Previous studies have investigated annular flow patterns experimentally and numerically. However, existing models remain insufficiently applicable to inclined annuli, and flow-pattern transition boundaries are often poorly defined.

Several studies have examined the flow behavior of annular multiphase flow. Because of experimental constraints, systematic investigations remain limited. Most previous studies focused on flow-pattern transitions and pressure-drop prediction in vertical wells, whereas inclined annuli have received less attention. Current wellbore pressure-drop calculations generally apply circular-pipe two-phase correlations directly to annular geometries.

Table 1 classifies representative studies by methodology and by the gap that remains for the present work. This concise comparison is intended to complement, rather than expand, the detailed narrative review below.

1.2.1. Flow Pattern Classification Methods

In 1982, Sadatomi [1] investigated the flow patterns and pressure drop of air–water flow in a vertical concentric annulus with a diameter ratio of 0.5. Three flow patterns were identified: bubbly, slug, and annular flow.

In 1989, Caetano et al. [2] conducted a systematic study of gas–liquid flow patterns in vertical annuli. They identified bubbly, dispersed-bubbly, slug, churn, and annular flow, modified Taitel's circular-pipe transition model for annular geometries, and presented flow-pattern maps for concentric and eccentric annuli.

In 1986, Hasan and Kabir [3] developed discrimination criteria for bubbly, slug, churn, and annular flow by analyzing flow-pattern transitions in vertical circular pipes.

In 1992, Hasan et al. [4] applied a drift-flux model to gas holdup in annular flow and predicted bubbly, slug, and churn flow in vertical and inclined annuli. They improved the Taylor-bubble rise-velocity correlation and obtained a more accurate gas-holdup relationship for inclined annuli.

In 2002, Lao et al. [5] noted that existing flow-pattern definitions were vague, classifications were inconsistent, and discrimination was often qualitative. They evaluated the applicability of classical flow-pattern maps to horizontal and vertical pipes and proposed a classification approach based on phase continuity.

In 2003, Zhang et al. [6] developed transition models for slug and annular flow in vertical annuli and investigated gas–liquid flow with a rotating inner tube.

In 2009, Gao et al. [7] performed laboratory experiments under high gas–liquid-ratio conditions to support the selection of flow-pattern prediction models for high-GLR wells.

In 2014, Lou et al. [8] adapted the Taitel–Dukler classification method to oil–water flow in horizontal pipes. They identified four regimes, including dispersed and stratified flows, and developed corresponding transition criteria and pressure-drop models.

In 2016, Chang et al. [9] used high-speed imaging to study gas–liquid flow in an adiabatic vertical pipe with an inner diameter of 50 mm. They extracted image features and applied hierarchical fuzzy reasoning to identify bubbly, plug, slug, and frothy flow.

In 2019, Liu et al. [10] developed an air–water experimental system containing horizontal, inclined, and vertical sections to represent a horizontal gas well. They identified five flow patterns and constructed a three-dimensional flow-pattern map using dimensionless gas–liquid velocities and inclination angle. A BP neural-network model was then used to predict wellbore flow patterns.

In 2021, Qiu [11] applied a VOF model to low-yield liquid-loading gas wells. The simulations showed a transition from bubbly to slug flow as gas holdup increased and identified the gas-holdup ranges associated with different flow patterns.

In 2022, Ji [12] compared conventional air–water flow with foam flow. Chen's flow-pattern map reproduced the foam-flow development reasonably well, and its transition boundary was modified using the experimental data.

Annular gas–liquid flow is classified in a manner similar to circular-pipe flow, with bubbly, dispersed-bubbly, slug, churn, and annular regimes commonly recognized. However, annular flow patterns differ substantially from those in circular pipes, particularly for slug and annular flow. Slug flow in an annulus contains two liquid films: the casing film adjacent to the casing wall and the tubing film adjacent to the tubing wall. These films must therefore be considered when interpreting flow-pattern transitions, especially for annular flow.

1.2.2. Pressure Drop Calculation Methods

In 1963, Duns and Ros [13] extended the analysis of gas–liquid flow in vertical tubes and proposed a dimensional-analysis-based pressure-gradient correlation.

In 1965, Hagedorn et al. [14] studied oil–gas–water flow in vertical wells with pipe diameters of 25.4, 31.75, and 38.1 mm. They modified the flow-resistance coefficient using the effective mixture density and developed a flow-pattern-independent pressure-gradient correlation with wide applicability to gas–liquid ratios.

In 1967, Orkiszewski [15] evaluated earlier pressure-gradient methods using data from 148 wells. The flow was divided into bubbly, slug, transition, and annular-mist regimes, and the most appropriate friction and holdup relationships were selected for each regime.

In 1972, Sanchez [16] applied the Duns–Ros and Hagedorn–Brown circular-pipe correlations to pressure-drop prediction in the annular space of oil wells.

In 1994, Ansari et al. [17] analyzed the flow mechanisms of bubbly, slug, churn, and annular flow in gas wells and developed pressure-prediction models for each regime.

In 2009, Liao et al. [18] evaluated six pressure-drop models for annular two-phase flow in drainage gas-recovery wells. The Hagedorn–Brown model produced the smallest average absolute error. They inferred liquid holdup from experimental data, corrected the Hagedorn–Brown holdup chart, and developed a modified model using a segmented correction equation.

In 2013, Qian et al. [19] used PIPSIM and measurements from 30 vertical wells in the Henan Oilfield to compare the Hagedorn–Brown, Mukherjee–Brill, Ansari, and Gray models. Their evaluation used mean relative error, mean absolute relative error, standard error, and relative performance coefficient.

In 2020, Zhang et al. [20] studied annulus-pressure buildup during unsteady testing of deepwater oil and gas wells. They developed a wellbore heat-transfer model that accounted for pressure- and temperature-dependent density and proposed a layered annulus-pressure calculation method.

In 2023, Xiong et al. [21] developed a VOF model for vertical annular gas–liquid flow in coalbed-methane wellbores. They examined the effects of gas content, inlet pressure, temperature, and pressure drop on flow patterns. Gas content was the dominant factor controlling flow-pattern transitions, whereas pressure and temperature had limited effects.

Table 1. Methodological comparison of representative annular-flow studies.

Study/Method	Geometry and Conditions	Main Contribution	Remaining Gap Relevant to This Study
Sadatomi et al. (1982) [1]; experiment	Vertical concentric annulus; diameter ratio 0.5	Flow-pattern and pressure-drop measurements for air–water flow.	No inclined or dual-size annulus comparison.
Caetano et al. (1989) [2]; experiment	Vertical concentric and eccentric annuli	Five flow patterns and modified transition diagrams.	Vertical geometry only; no transient CFD comparison.
Hasan and Kabir (1992) [3]; model/experiment	Vertical and inclined annuli	Drift-flux holdup formulation and Taylor-bubble modification.	Limited integration with quantitative transient pressure-drop simulation.
Zhang et al. (2003) [6]; model	Vertical concentric annulus	Gas-holdup and pressure-drop prediction for annular flow.	Does not resolve the two liquid films in an inclined geometry.
Liu et al. (2019) [10]; experiment/model	Horizontal-well pipe section	Flow-pattern map and neural-network prediction.	Not specific to an annulus or dual liquid films.
Qiu (2021) [11]; numerical	Low-yield gas well; VOF	Transient flow-pattern evolution under liquid loading.	Circular wellbore geometry and no matched dual-size annulus experiment.
Xiong et al. (2023) [21]; numerical	Vertical annular pipe; VOF	Effects of gas content, pressure, and temperature.	No inclined dual-size experiment or regime-specific pressure-drop validation.

Numerical simulation has become increasingly important in multiphase-flow research and can reduce the cost of experimental investigations. Nevertheless, pressure-drop studies of deviated gas wells still rely mainly on experiments, and numerical studies of inclined annular flow remain limited.

Most established gas–liquid pressure-drop models were developed from experimental data, mechanistic analysis, and empirical experience. Each model therefore has a limited range of applicability and cannot reliably predict every flow condition. In addition, most pressure-drop data were obtained from vertical wells, while measurements for inclined wells remain scarce.

Taken together, the literature shows a consistent gap: experimental studies have established annular flow-pattern transitions mainly in vertical geometries, while numerical VOF studies rarely provide a matched dual-size, inclined, air–water experiment with regime-specific pressure-drop comparison. The dual liquid films and the change in annular clearance can modify both interface organization and frictional pressure loss, but these effects are seldom examined within one coherent dataset. The present study addresses that gap by using a common 5 m geometry in the experiment and simulation, by comparing the three dominant regimes separately, and by reporting the remaining validation limitations instead of treating agreement with the authors' own data as universal validation.

1.3. Proposed Research Content

This study provides a matched experimental and CFD dataset for two annular clearances at 45° and 90°, regime-specific comparisons of bubbly, slug, and annular flow, and a pressure-drop assessment of the newly developed annular multiphase correlation against

established models. The "New Model" denotes this fitted flow-pattern-specific correlation, not the CFD prediction alone.

2. Experimental and Numerical Simulation Methods

2.1. Experimental Design

The experiments used the multiphase pipe-flow platform and the annular multiphase-flow test system (Figure 1). Gas and liquid flow rates were regulated by an air compressor and a plunger pump, respectively, while flow patterns, pressure difference, and liquid holdup were recorded.

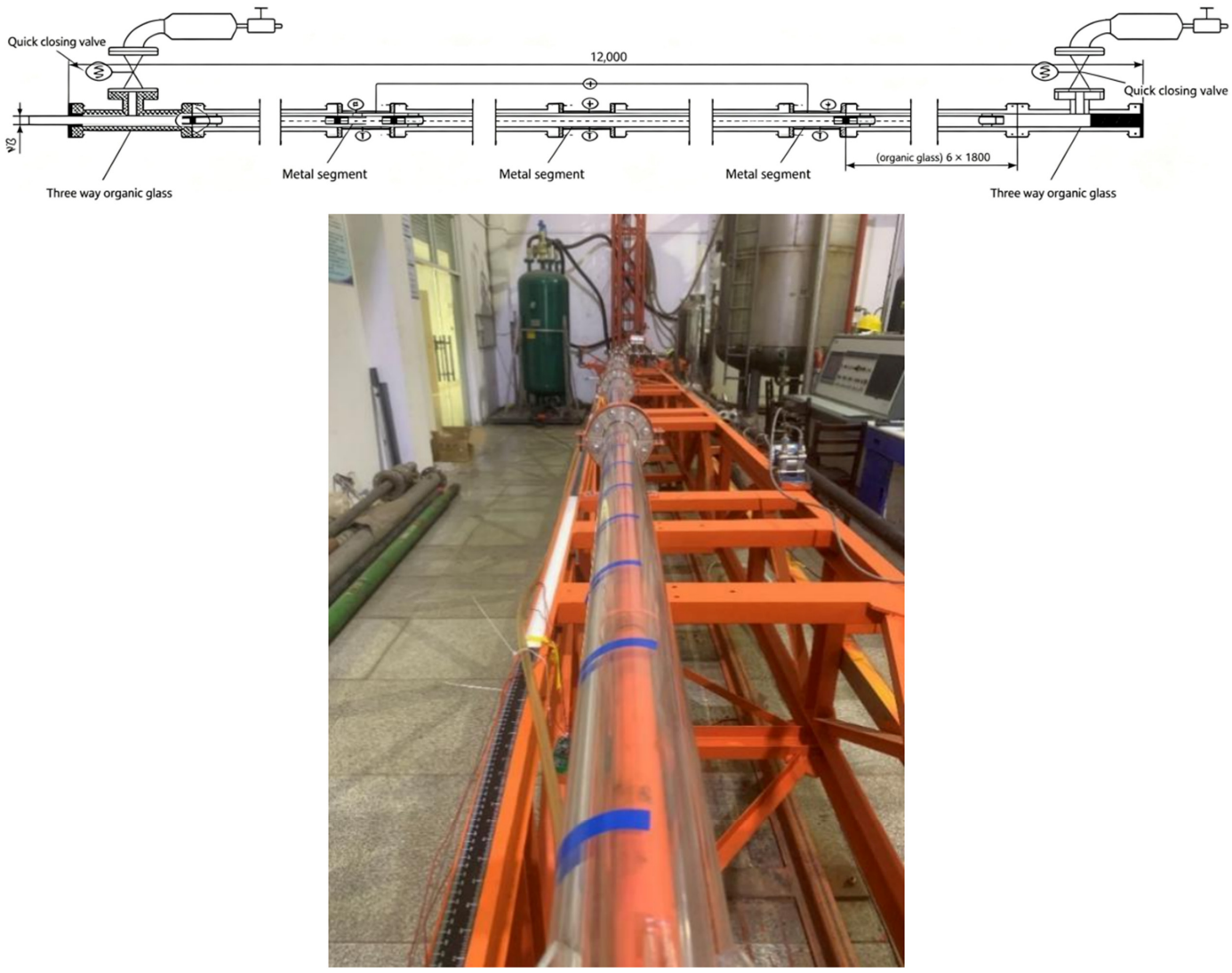


Figure 1. Schematic of the laboratory annular multiphase-flow loop. The simulation and pressure-drop comparison section is 5 m long.

2.1.1. Experimental Setup

The core experimental setup is an adjustable annular pipe system with a 5 m test section, a tubing outer diameter of 38.5 mm, and casing inner diameters of 75.9 and 62 mm. The gas and liquid inlets use independent velocity control. The adjustable support permits the test section to be set at the intended inclination angle.

The experiments were conducted at ambient pressure and temperature (0.101 MPa and 20 °C). Pressure and temperature were not varied as independent test variables. Following

the procedures reported by Liu et al. [22], the pressure sensor had a range of 0–3.5 MPa and an error of ±0.1%; the temperature sensor had a range of 0–90 °C and an error of ±0.5%; liquid and gas flow rates had errors of ±0.3% and ±1%, respectively. The reported uncertainties were within ±2% for total pressure drop, ±5% for liquid holdup, and approximately 5.4% for friction pressure drop.

2.1.2. Data Acquisition

Differential-pressure sensors with an accuracy of ±0.25% were used to obtain the pressure gradient. Flow morphology was recorded by a high-speed camera at 1000 frames/s, and liquid holdup was measured by the conductivity-probe method. The same instrumentation and acquisition procedure were used for all test conditions.

2.2. Numerical Simulation Settings

2.2.1. Model Construction

A three-dimensional model of the 5 m measurement section was constructed in SpaceClaim (Figure 2). Structured hexahedral grids were generated in ICEM. Four systematically refined grids were evaluated at Vsl = 0.3268 m/s, Vsg = 4.085 m/s, and an inclination angle of 90°. The resulting pressure gradients are summarized in Table 2 and Figure 3. The change between the 895,645-cell and 1,035,752-cell meshes was 0.92%; therefore, the 895,645-cell mesh was used for the production simulations. This mesh check used one representative annular-flow condition; comprehensive mesh sensitivity across all flow regimes is recommended for future work.

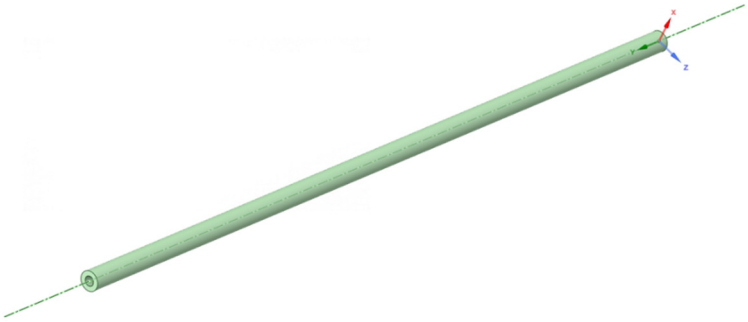


Figure 2. Geometric model of the pipe.

Table 2. Grid-independence results.

Mesh	Number of Cells	Pressure Gradient (Pa/m)
Mesh 1	653,048	3486.74
Mesh 2	724,685	3575.35
Mesh 3	895,645	3750.58
Mesh 4	1,035,752	3785.26

The numerical settings were a time step of 0.001 s, a maximum of 20 iterations per time step, a maximum residual of 0.001, and a simulated physical time of 10 s. A separate time-step-independence study and a Courant-number sensitivity study were not performed; these are stated as limitations.

The computational domain used the same pipe length, tubing outer diameter, and casing inner diameters as the experiments. The inlet was placed upstream of the measurement interval, and a pressure outlet was used at the downstream boundary. These settings ensure that the simulated and measured sections are directly comparable.

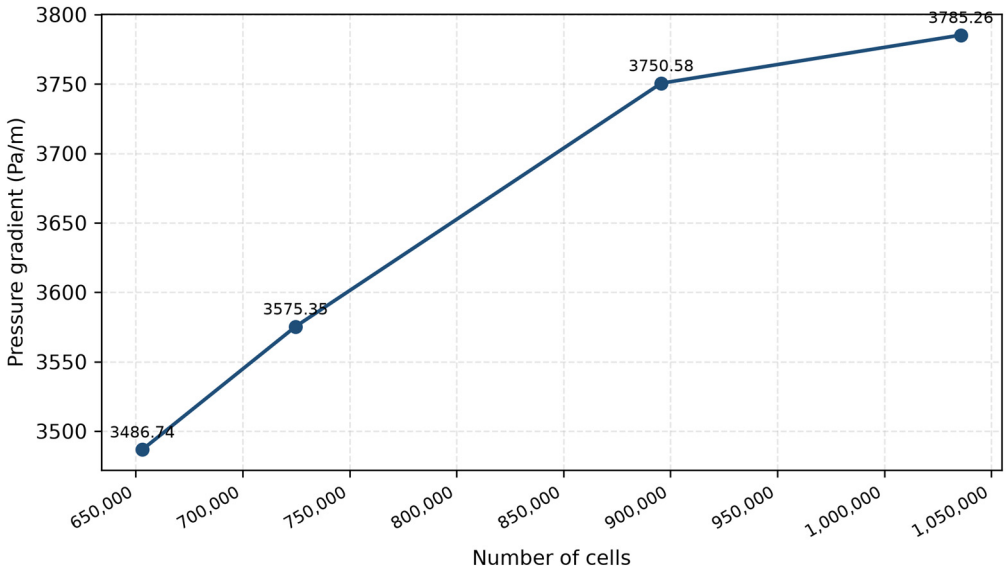


Figure 3. Grid-independence results at Vsl = 0.3268 m/s, Vsg = 4.085 m/s, and 90°.

2.2.2. Solution Parameters

The gas phase was set as the primary phase and the liquid phase as the secondary phase in Fluent. VOF was selected because a distinct gas–liquid interface exists and because VOF tracks the volume fraction of each phase within each computational cell. Mixture and Eulerian formulations were not selected for the present interface-resolving analysis [23,24]. The gas Reynolds number ranged from 6.92×10^5 to 8.4×10^6, confirming fully turbulent conditions. RNG k-ε was used because it improves the baseline accuracy of the standard k-ε model for the present annular-flow conditions. No direct comparative simulation was performed with realizable k-ε or SST k-ω, and the manuscript does not claim a general superiority of RNG k-ε.

2.2.3. Turbulence-Model Selection

The model descriptions and implementation follow the ANSYS Fluent Theory Guide (v.2023). RNG k-ε was selected because it improves the baseline accuracy of standard k-ε for the present conditions and is based on renormalization-group theory [25]. Standard k-ε remains a widely used baseline. Realizable k-ε improves specific realizability constraints, and SST k-ω provides improved near-wall performance but generally requires finer near-wall resolution [26]. No additional CFD simulations with alternative turbulence models were performed.

Because this work focuses on flow morphology, integral pressure drop, and a tractable transient simulation, RNG k-ε provides an appropriate modeling-level compromise. The lack of direct model-to-model simulations is identified as a limitation rather than presented as completed validation.

2.3. Annular Multiphase Pressure-Drop Correlation

The "New Model", whose closure relations and fixed parameters are summarized in Table 3, is a flow-pattern-specific pressure-drop correlation developed for annular gas-liquid flow, not the CFD solution itself. The correlation was formulated from 334 experimental cases and supporting CFD analysis for two annular geometries. The tested ranges were liquid flow rates of 20–300 m^3/d and gas flow rates of 5000–50,000 m^3/d at inclination angles of 30°, 45°, 60°, and 90°.

Table 3. Closure relations and fixed parameters used in the New Model.

Flow Regime	Final Pressure-Gradient Equation	Closure Relation	Fixed Parameters and Coefficients
Bubbly	Equation (2)	Drift-flux slip relation with the Harmathy bubble-rise velocity and the Wallis swarm correction; $\rho_s = \rho_L H_L + \rho_G(1 - H_L)$.	n = 0.5; rise-velocity coefficient = 1.53; annular-pipe friction correction applied.
Slug/churn	Equations (3) and (4), including the mixture-density relation	Modified slug-flow pressure-gradient formulation; Chokshi void-fraction relation; annular-pipe turbulent friction factors.	1.126 and 1.41 in the void-fraction closure; exponent 0.25; $\lambda = \frac{C_t Re^{-0.25}}{15}$ (slug); $\lambda = \frac{C_t Re^{-0.25}}{25}$ (churn).
Annular	Equations (5) and (6)	Two-film force balance with Wallis droplet entrainment and interface-friction closures.	$F_e = 1 - \exp[-0.125(\phi - 1.5)]$; $\phi = 10^4 U_{sG} \frac{\mu_G}{\sigma} \left(\frac{\rho_G}{\rho_L}\right)^{\frac{1}{2}}$; p = 7; $\frac{u}{u_{max}} = 0.874$; $f_{oi} = f_o\left(1 + 300\frac{\Delta_o}{d_2}\right)$.

Note: For slug/churn flow, $N = d_1/d_2$, $C_{lo} = 64$, and $C_{to} = 0.316$. The structural-coefficient ratios are given in Equations (7) and (8).

Separate closures are used for bubbly flow, slug/churn flow, and annular flow.

The reduced pressure-gradient formulation used by the New Model is given below. Only the final closure equations required to reproduce the reported calculations are included.

The total pressure gradient is decomposed into friction, gravitational, and acceleration components:

$$-\left(\frac{dP}{dz}\right)_t = \left(\frac{dP}{dz}\right)_f + \left(\frac{dP}{dz}\right)_G + \left(\frac{dP}{dz}\right)_A \quad (1)$$

For bubbly flow, the pressure gradient is calculated as

$$\left(\frac{dP}{dz}\right) = \rho_s g + \frac{4f}{(d_2 - d_1)} \rho_s \frac{(U_{SL} + U_{SG})^2}{2} \quad (2)$$

For slug/churn flow, the pressure gradient is calculated as

$$\left(\frac{dp}{dL}\right) = \rho_M g \sin\theta + \frac{\lambda \rho_M U_M^2}{2 d_h} \quad (3)$$

$$\rho_M = \rho_L H_L + \rho_G(1 - H_L) \quad (4)$$

For annular flow, the pressure gradient is calculated as

$$\left(\frac{dP}{dL}\right)_t = [\alpha \rho_G + (1 - \alpha)\rho_L] g \sin\theta + \left(\frac{dp}{dx}\right)_f \quad (5)$$

and the void fraction is closed by

$$\alpha = \frac{(r_2 - \Delta_o)^2 - (r_1 + \Delta_i)^2}{r_2^2 - r_1^2} \left(1 - \frac{U_{SL} Fe}{U_{SL} Fe + U_{SG}}\right) \quad (6)$$

Here, P is pressure; z, L, and x are axial coordinates; g is gravitational acceleration; $U_s L$ and $U_s G$ are the superficial liquid and gas velocities; $U_M = U_s L + U_s G$; ρ_L and ρ_G are the phase densities; ρ_M and ρ_s are mixture densities; ρ_M is used for slug/churn flow and $\rho_s = \rho_L H_L + \rho_G(1 - H_L)$ is used for bubbly flow; H_L is liquid holdup, with $H_L = 1 - \alpha$; α is void fraction; θ is inclination angle; d_h is hydraulic diameter; d_1 and d_2 are the inner and

outer diameters; r_1 and r_2 are the inner and outer radii; Δ_I and Δ_o are the inner and outer liquid-film thicknesses; F_e is the droplet entrainment fraction; f is the friction factor; λ is the two-phase friction factor; Re is Reynolds number; C_t is the annular-pipe friction correction coefficient; μ_G is gas viscosity; σ is surface tension; φ is the dimensionless gas number used by the Wallis entrainment closure; u is the mean liquid-film velocity; u_{max} is its maximum value; f_o and f_{oi} are the single-phase wall and gas–liquid interface friction factors; n and p are the Wallis swarm and film-velocity profile exponents, respectively. The subscripts t, f, G, and A denote the total, frictional, gravitational, and acceleration components, respectively.

The flow-pattern-specific closure relations and fixed parameters are summarized in Table 3.

$$\frac{C_l}{C_{lo}} = \frac{(1-N)^2}{\left[\frac{1-N^4}{1-N^2} - \frac{1-N^2}{\ln(1/N)}\right]} \quad (7)$$

$$\frac{C_t}{C_{to}} = \frac{C_t}{0.316} = \sqrt[3]{0.0154\frac{C_l}{C_{lo}} - 0.012} + 0.85 \quad (8)$$

C_t is then used in the friction-factor expressions for slug and churn flow given in Table 3.

The project report evaluated the correlation over the complete 334-case dataset and reported an average relative error of 1.32% and an average absolute error of 7.86%. The corresponding results for the current experimental dataset are reported in Section 3.2.

3. Results and Analysis

3.1. Comparison of Flow Pattern Characteristics

The flow-pattern results are summarized in Table 4. Classification was based on the spatial distribution of the gas phase in synchronized images: bubbly flow contains discrete bubbles in a continuous liquid phase, slug flow contains alternating gas pockets and liquid slugs, and annular flow contains a continuous gas core surrounded by liquid films on both walls.

Table 4. Regime-specific summary of representative experimental and numerical results.

Flow Regime	Representative Inlet Conditions	Observed and Simulated Characteristics	Quantitative Indicator
Bubbly	Air 0.295 m/s; water 1.77 m/s; 45° and 90°; both casing sizes	Bubbles concentrate away from the walls; gas fraction remains below 0.2; morphology is reproduced by the VOF model.	The bubble structures are visibly larger in the 3-1/2 in tubing than in the 2-7/8 in tubing.
Slug	Air 2.00 m/s; water 1.20 m/s; 90°; both casing sizes	Alternating Taylor bubbles and liquid slugs; the inclined-pipe interface and the inner/outer films are asymmetric.	The liquid-film distribution is visibly non-uniform in the inclined test section.
Annular	Air 3.00 m/s; water 0.20 and 2.00 m/s; 90°; both casing sizes	A continuous gas core is bounded by inner and outer liquid films; the simulated interface follows the observed structure.	The outer-wall liquid film is visibly thicker than the inner-wall film.

3.1.1. Bubbly Flow

Both experiments and simulations show that bubbles concentrate near the center of the annulus (Figure 4), with cross-sectional gas content below 0.2. The bubble structures are visibly larger in the 3-1/2 in tubing than in the 2-7/8 in tubing (Figure 5). Similar bubbly structures are observed at 45° in the 2-7/8 in tubing (Figure 6). The corresponding 3-1/2 in tubing case shows comparable bubbly structures at 45° (Figure 7).

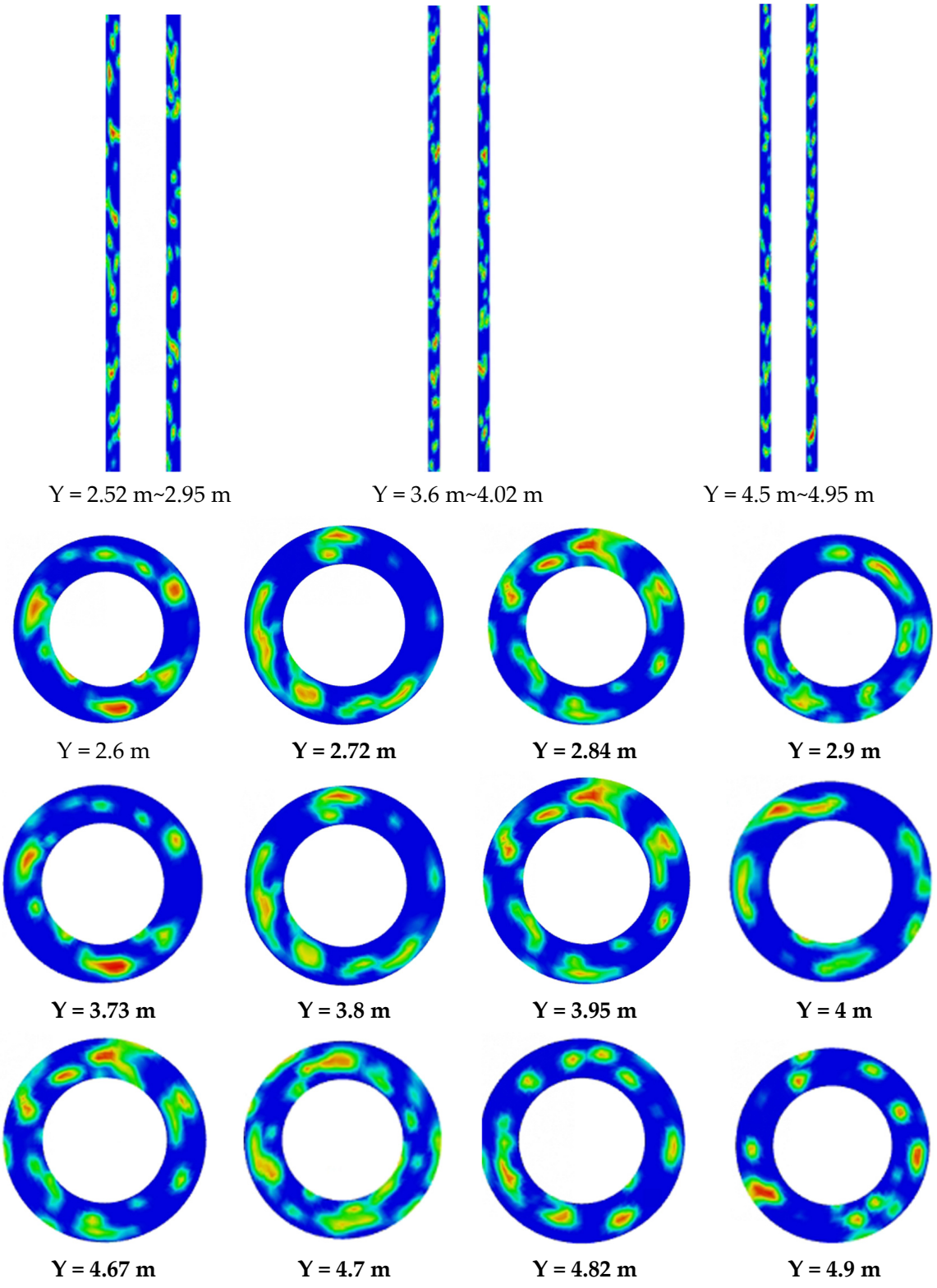


Figure 4. Air: 0.295 m/s, water: 1.77 m/s, axial and cross-sectional contour maps of bubbly flow (1-1/2″ coiled tubing, 2-7/8″ tubing, 90°). The color scale represents the gas volume fraction; blue indicates low gas content, green and yellow indicate intermediate gas content, and red indicates high gas content.

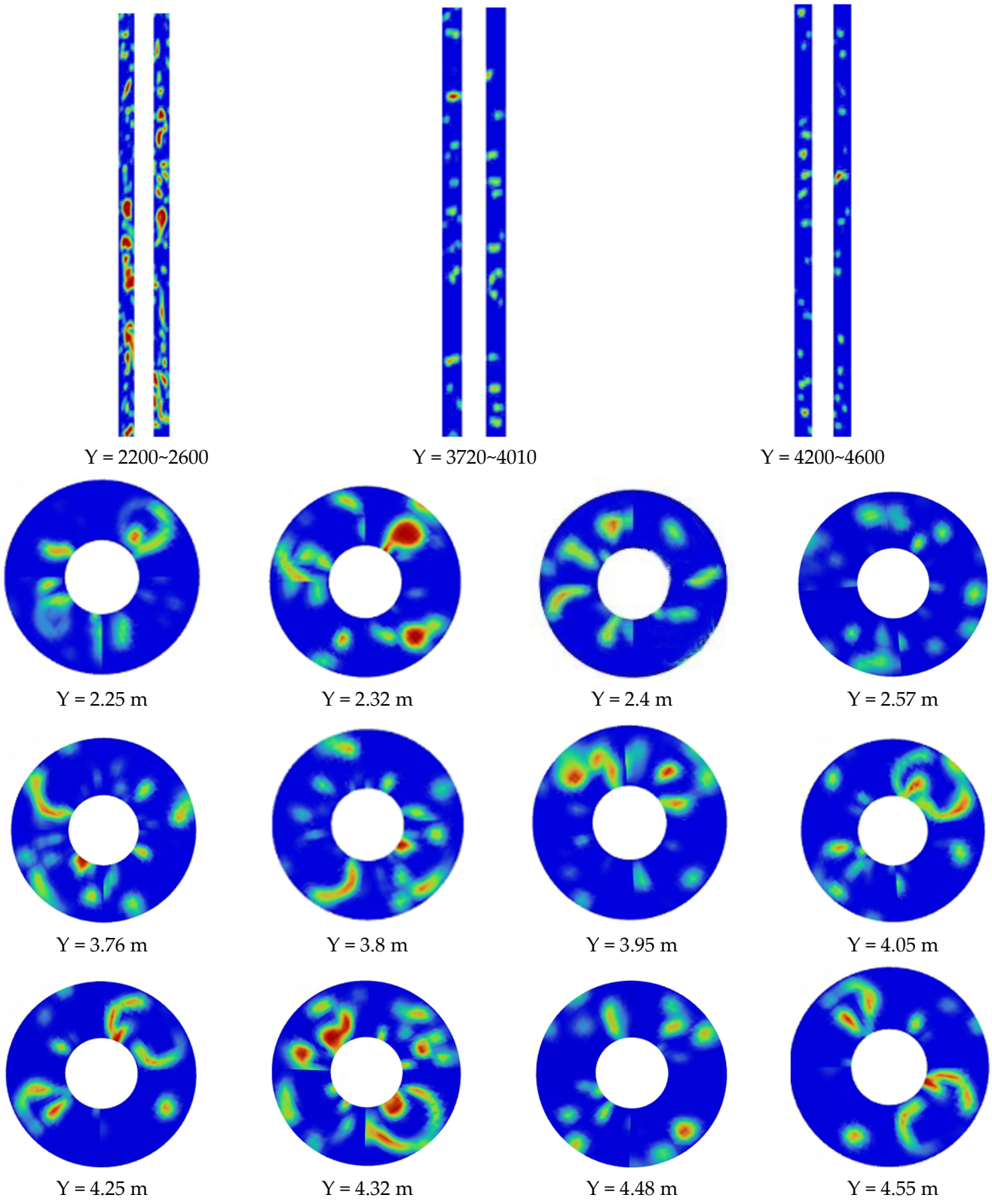


Figure 5. Air: 0.295 m/s, water: 1.77 m/s, axial and cross-sectional contour maps of bubbly flow (1-1/2″ coiled tubing, 3-1/2″ tubing, 90°). The color scale represents the gas volume fraction; blue indicates low gas content, green and yellow indicate intermediate gas content, and red indicates high gas content.

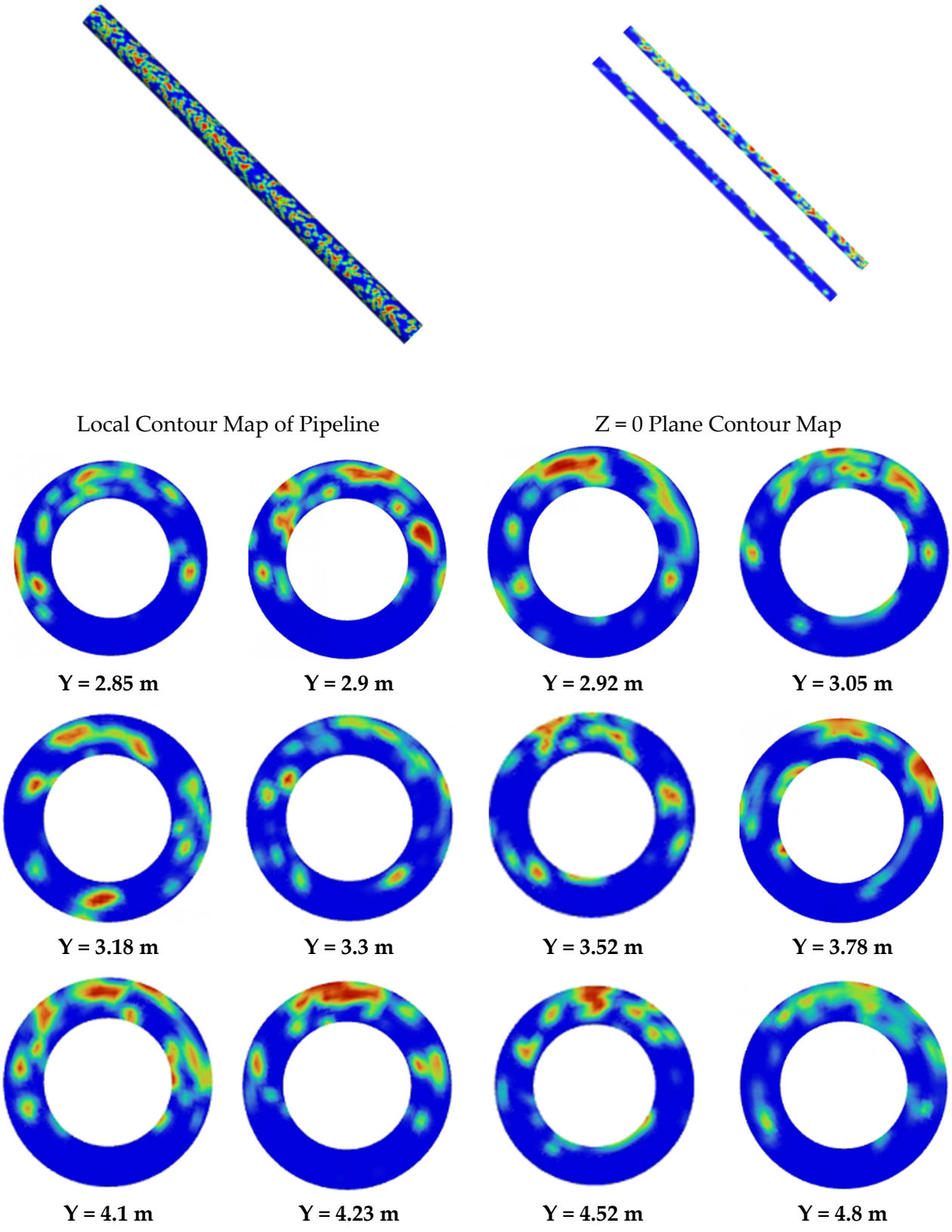


Figure 6. Air: 0.295 m/s, water: 1.77 m/s, axial and cross-sectional contour maps of bubbly flow (1-1/2″ coiled tubing, 2-7/8″ tubing, 45°). The color scale represents the gas volume fraction; blue indicates low gas content, green and yellow indicate intermediate gas content, and red indicates high gas content.

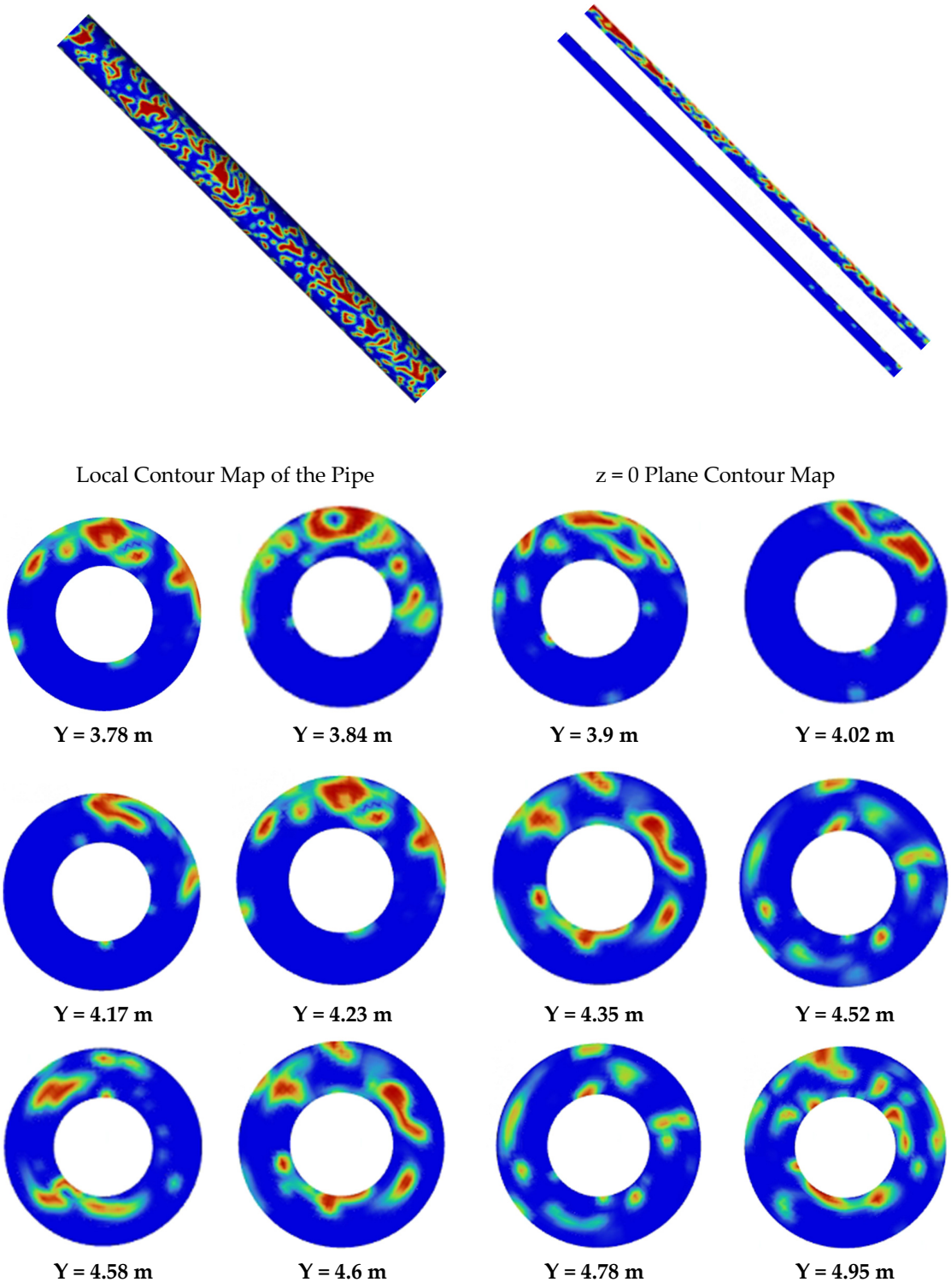


Figure 7. Air: 0.295 m/s, water: 1.77 m/s, axial and cross-sectional contour maps of bubbly flow (1-1/2″ coiled tubing, 3-1/2″ tubing, 45°). The color scale represents the gas volume fraction; blue indicates low gas content, green and yellow indicate intermediate gas content, and red indicates high gas content.

3.1.2. Slug Flow

Taylor bubbles and liquid slugs alternate prominently, and the gas–liquid interface is asymmetric in the inclined pipe (Figure 8). The liquid-film distribution is visibly non-uniform. The corresponding 3-1/2 in tubing case shows similar alternating Taylor-bubble and liquid-slug structures (Figure 9).

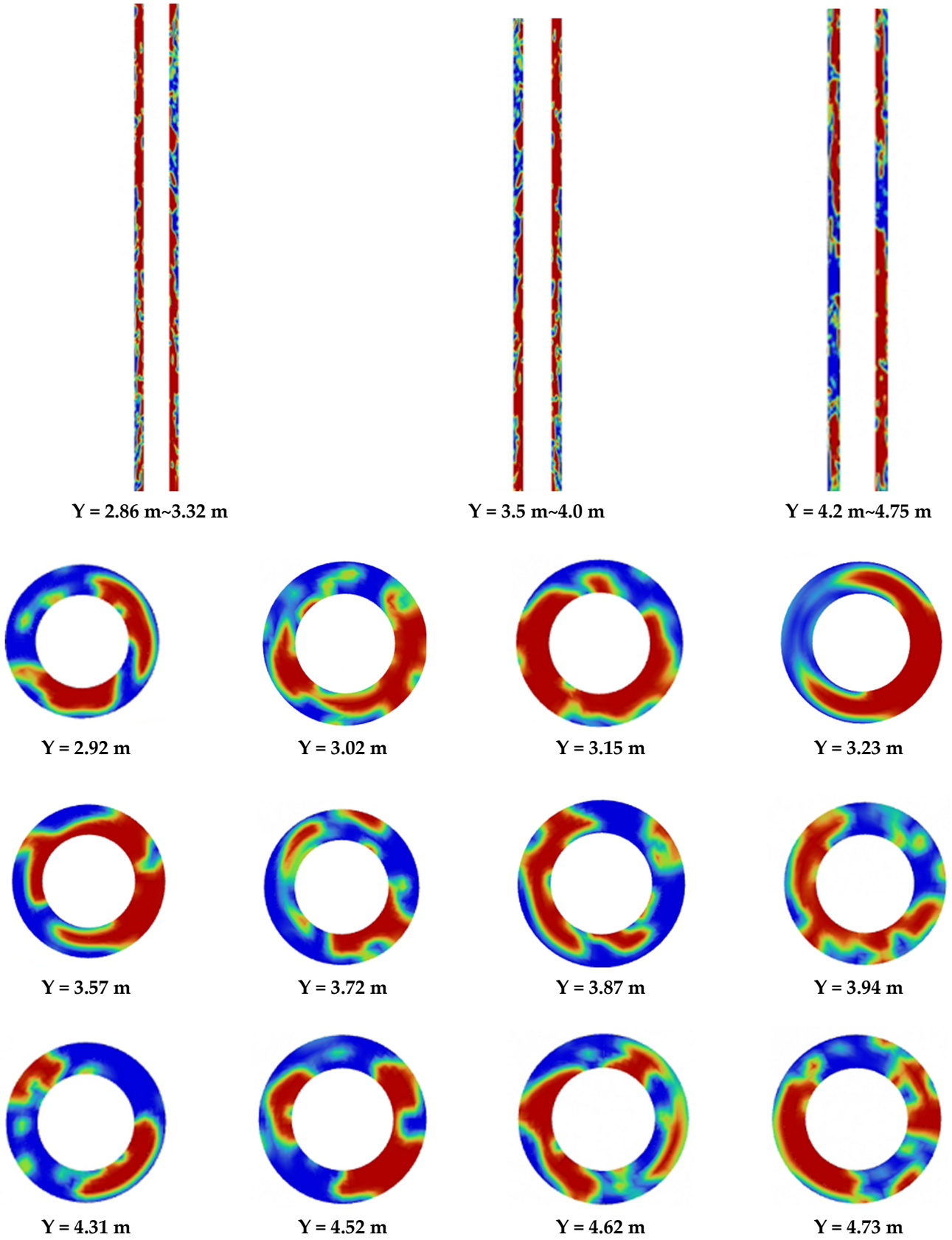


Figure 8. Air: 2 m/s, water: 1.2 m/s, axial and cross-sectional contour maps of slug flow (1-1/2″ Coiled tubing, 2-7/8″ tubing, 90°). The color scale represents the gas volume fraction; blue indicates low gas content, green and yellow indicate intermediate gas content, and red indicates high gas content.

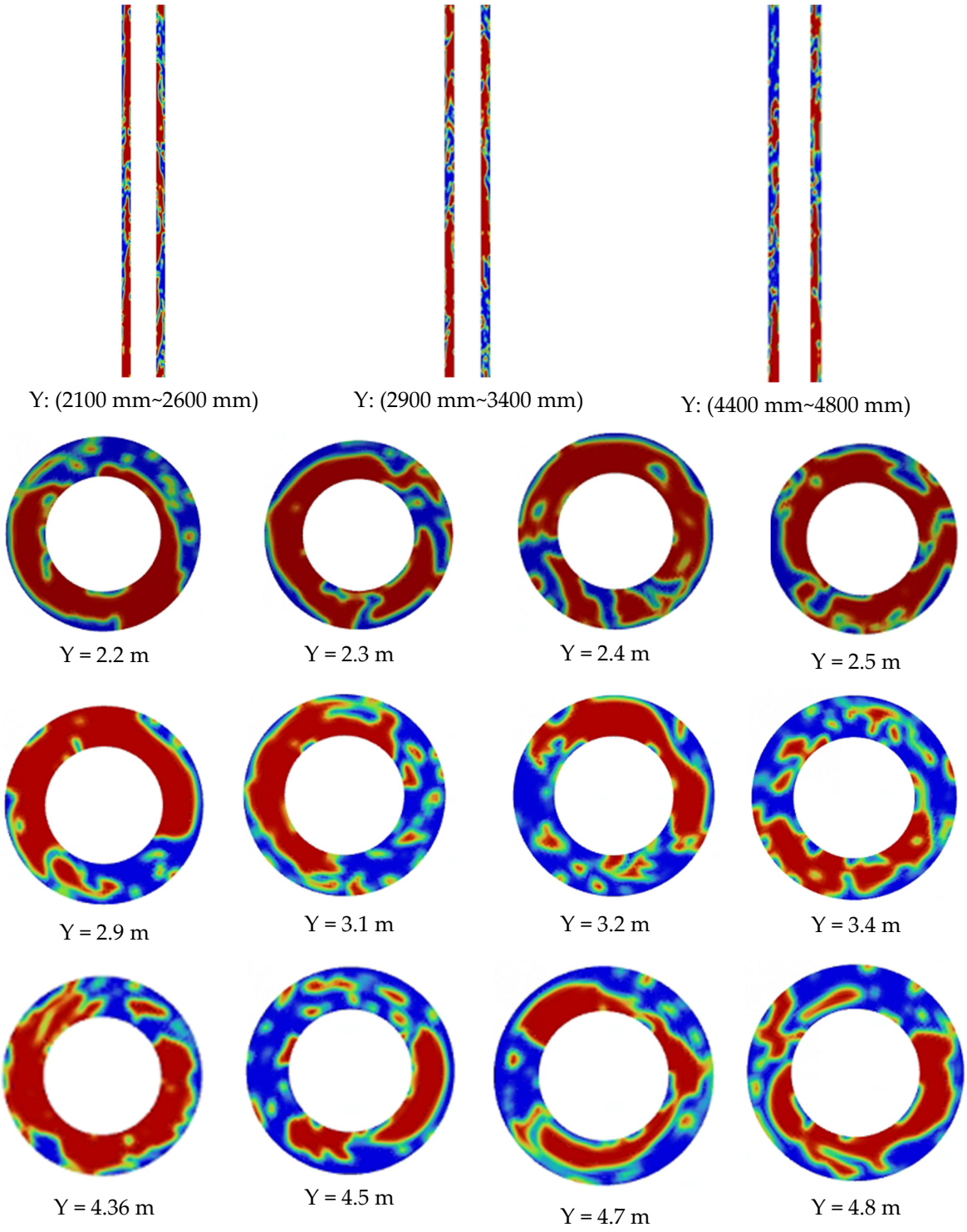


Figure 9. Air: 2 m/s, water: 1.2 m/s, axial and cross-sectional contour maps of slug flow (1-1/2″ coiled tubing, 3-1/2″ tubing, 90°). The color scale represents the gas volume fraction; blue indicates low gas content, green and yellow indicate intermediate gas content, and red indicates high gas content.

3.1.3. Annular Flow

The outer-wall liquid film is visibly thicker than the inner-wall film (Figure 10). The film becomes less stable when the gas-core velocity exceeds 3 m/s. The corresponding 3-1/2 in tubing case exhibits a similar two-film structure (Figure 11).

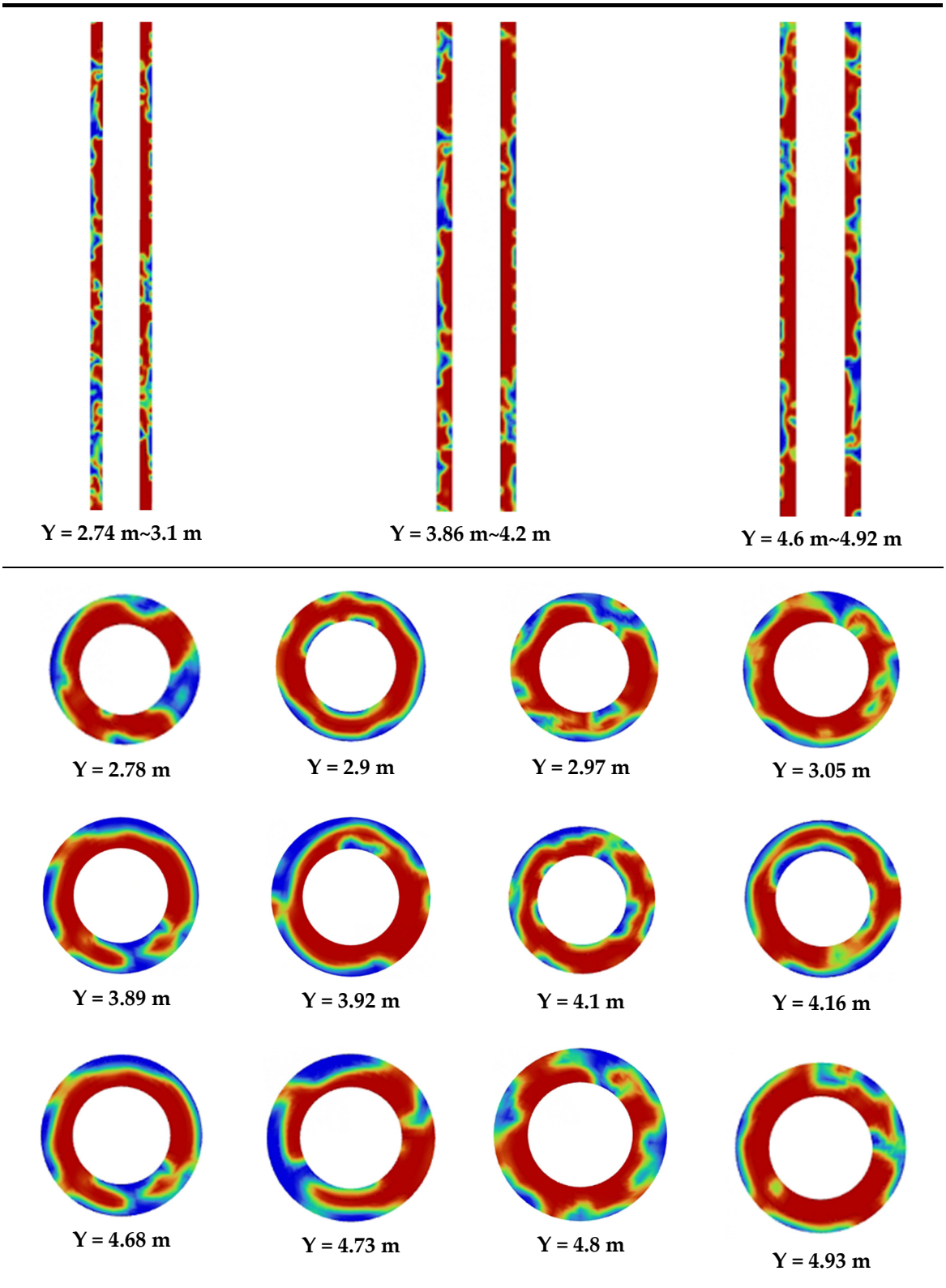


Figure 10. Air: 3 m/s, water: 0.2 m/s, axial and cross-sectional contour maps of annular flow (1-1/2″ coiled tubing, 2-7/8″ tubing, 90°). The color scale represents the gas volume fraction; blue indicates low gas content, green and yellow indicate intermediate gas content, and red indicates high gas content.

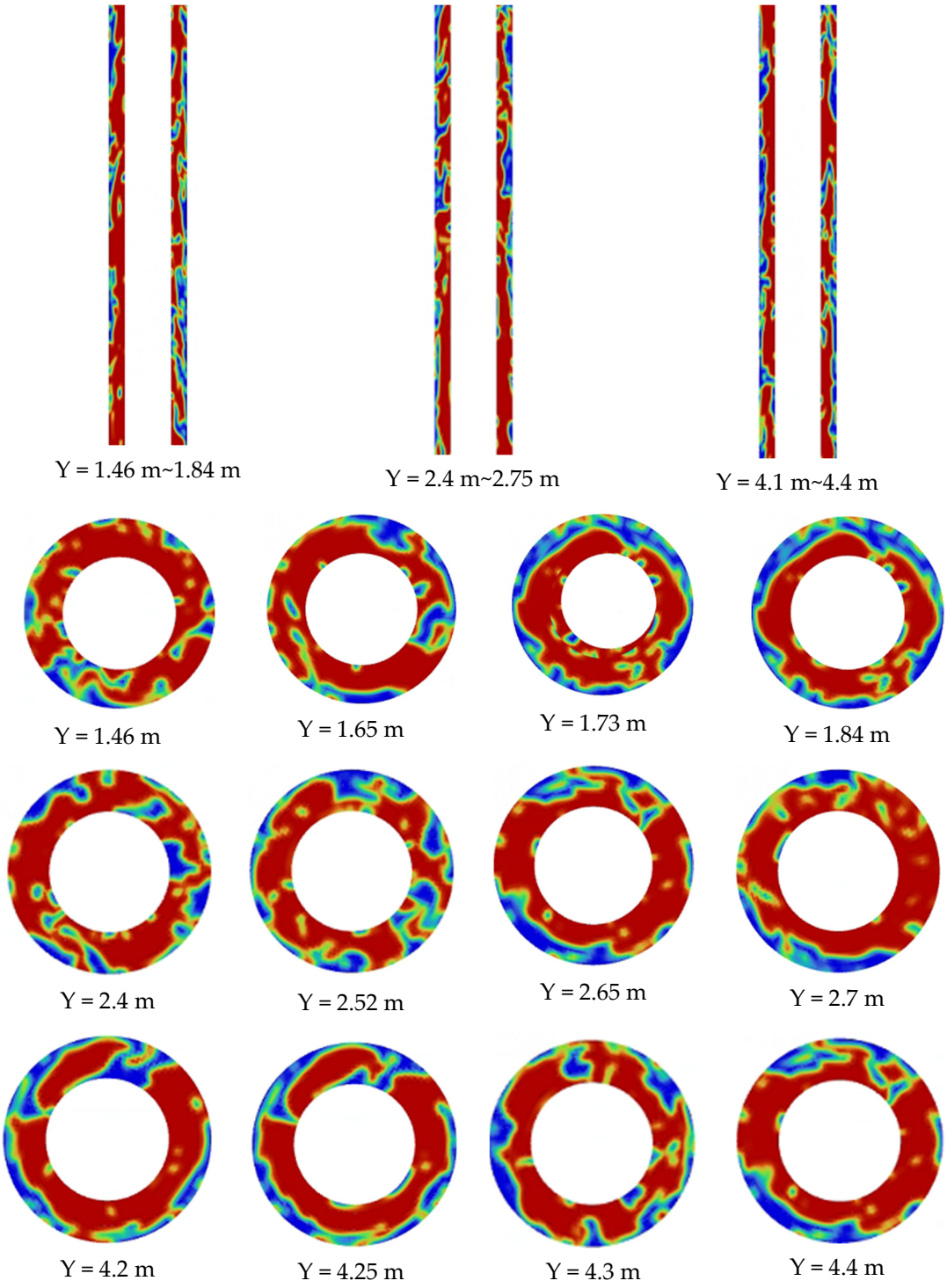


Figure 11. Air: 3 m/s, water: 2 m/s, axial and cross-sectional contour maps of annular flow (1-1/2″ coiled tubing, 3-1/2″ tubing, 90°). The color scale represents the gas volume fraction; blue indicates low gas content, green and yellow indicate intermediate gas content, and red indicates high gas content.

3.2. Pressure-Drop Prediction and Model Comparison

The error analysis between simulated and measured pressure drop gives $R^2 = 0.92$, with an average relative error of 1.07% and an average absolute error of 7.91% (Table 5; Figure 12). The Beggs-Brill, Mukherjee, Aziz, Hasan, and JPI correlations have average absolute errors of 56.86%, 22.45%, 68.23%, 43.84%, and 40.61%, respectively.

Table 5. Errors between predictions of different models and experimental values.

Model.	New Model	Beggs-Brill	Mukherjee	Aziz	Hasan	JPI
Average Relative Error (%)	1.07	56.86	3.18	28.75	43.69	49.65
Average Absolute Error (%)	7.91	56.86	22.45	68.23	43.84	40.61

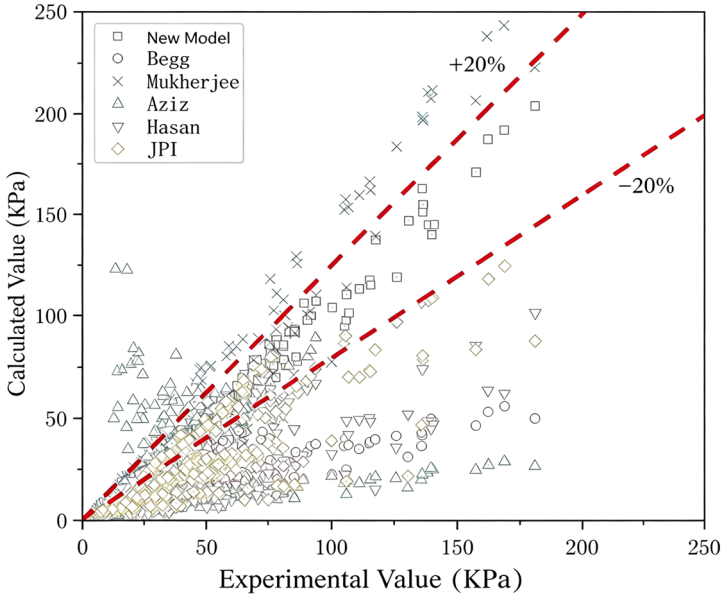


Figure 12. Comparison of predicted and experimental pressure-drop values.

3.3. Error Analysis

The flow-pattern correlation correctly classified 304 of 334 experimental cases, corresponding to 91% overall accuracy. Misclassifications were concentrated near the slug-churn and churn-annular boundaries, where gas–liquid mixing and transition hysteresis reduce boundary sharpness.

3.4. Comparison with Published Annular-Flow Observations

Previous experimental studies of vertical annuli have reported bubbly, slug/churn, and annular flow regimes and the presence of liquid films [1,2], while studies of inclined annuli have focused on holdup and transition behavior [4]. The flow-regime sequence observed in the present study follows the same general sequence. Under inclined conditions, the simulated liquid film is non-uniform and thicker on the outer wall, which is consistent with the two-film behavior reported for annular-flow experiments [2]. The present measurements also show that pressure drop increases with liquid flow rate and exhibits a non-monotonic response to gas flow rate, following the general regime-dependent pressure-drop behavior reported in two-phase inclined and annular-flow studies [1,2]. However, the published datasets differ in annular geometry, inclination, fluid properties, and velocity range, so they do not provide a fully matched quantitative benchmark. The comparison is therefore qualitative, while quantitative external validation remains future work.

4. Conclusions

(1) A matched experimental and three-dimensional transient VOF study was performed for air–water annular flow in a 5 m test section with a 38.5 mm tubing outer diameter and casing inner diameters of 75.9 and 62 mm. The tests covered air velocities of 0.295–3.00 m/s and water velocities of 0.20–2.00 m/s at inclinations of 45° and 90°.

(2) The simulated bubbly, slug, and annular morphologies agree with the experimental records. Bubbles concentrate away from the walls in bubbly flow, Taylor bubbles alternate with liquid slugs in slug flow, and a continuous gas core bounded by inner and outer films develops in annular flow. The outer-wall film is visibly thicker than the inner-wall film and becomes less stable above a gas-core velocity of 3 m/s.

(3) The newly developed annular multiphase pressure-drop correlation reproduces the measured pressure-drop trend with $R^2 = 0.92$ and an average absolute error of 7.91% for the present experimental dataset. The full 334-case project validation produced average relative and absolute errors of 1.32% and 7.86%, respectively.

(4) The main limitations are the ambient air–water test conditions, two annular clearances, two inclination angles, and the absence of independent entrainment measurements and complete spatiotemporal holdup profiles. The mesh-convergence check used one representative annular-flow condition, and no separate time-step, Courant-number, or direct turbulence-model comparison was performed. The flow-pattern correlation classified 304 of 334 cases correctly (91%), with errors concentrated near the slug-churn and churn-annular boundaries.

(5) Future work should extend the test matrix to additional pressures, temperatures, inclination angles, and annulus aspect ratios; include independent droplet-entrainment and spatiotemporal holdup measurements; compare RNG k-ε, realizable k-ε, and SST k-ω under identical mesh conditions; and test the established correlation against independent published annular-flow datasets.

Author Contributions: Conceptualization, H.J.; Methodology, H.J., W.L. (Wei Li) and W.L. (Wei Luo); Software, Q.L. and W.L. (Wei Luo); Validation, W.L. (Wei Li), J.S. and J.W.; Formal analysis, H.J., C.K., J.S., Q.L. and W.L. (Wei Luo); Investigation, H.J., W.L. (Wei Li), C.K., J.S. and Q.L.; Resources, J.S. and B.M.; Data curation, W.L. (Wei Li), C.K. and J.W.; Writing—review and editing, H.J., W.L. (Wei Li), C.K., B.M. and J.W.; Visualization, H.J., C.K. and Q.L.; Project administration, B.M. All authors have read and agreed to the published version of the manuscript.

Funding: This research received no external funding.

Data Availability Statement: The original contributions presented in this study are included in the article. Further inquiries can be directed to the corresponding author.

Conflicts of Interest: Authors Hongtao Jing, Wei Li, Chang'e Kong, Jianxin Shen, Qisong Lei were employed by the PetroChina Tarim Oilfield Company. Bin Ma was employed by the PetroChina Tuha Oilfield Company. The remaining authors declare that the research was conducted in the absence of any commercial or financial relationships that could be construed as a potential conflict of interest. These companies had no role in the design of the study, the collection, analysis, or interpretation of data, the writing of the manuscript, or the decision to publish the results.

References

1. Sadatomi, M.; Sato, Y.; Saruwatari, Y. Two-Phase Flow in Vertical Noncircular Channels. *Int. J. Multiph. Flow* **1982**, *8*, 641–655. [CrossRef]
2. Caetano, E.F.; Shoham, O.; Brill, J.P. Upward Vertical Two-phase Flow through an Annulus—Part 1: Single-phase friction factor, Taylor bubble rise velocity and flow pattern prediction. In *Multiphase Flow: Proceedings of the 4th International Conference*; BHRA: Cranfield, UK, 1989; pp. 301–330.
3. Hasan, A.R.; Kabir, C.S. A Study of Multiphase Behavior in Vertical Oil Wells: Part I—Theoretical Treatment. *SPE* **2008**, *1986*, 263–272.
4. Hasan, A.R.; Kabir, C.S. Two-phase flow in vertical and inclined annuli. *Int. J. Multiph. Flow* **1992**, *18*, 279–293. [CrossRef]
5. Lao, L.; Zheng, Z.; Wu, Y.; Li, D. Some Issues on Gas-Liquid Two-Phase Flow Patterns and Their Identification. *Adv. Mech.* **2002**, *32*, 235–249.
6. Zhang, J.; Chen, T.; Wen, J.; Luo, T. Prediction of Gas Holdup and Pressure Drop for Upward Gas-Liquid Annular Flow in Vertical Concentric Annular Pipes. *CIESC J.* **2003**, *54*, 47–51.

7. Gao, Q.; Li, T.; Yang, R. Study on Flow Pattern Identification of Vertical Two-Phase Pipe Flow with High Gas-Liquid Ratio. *Petrochem. Ind. Appl.* **2009**, *28*, 19–21.
8. Chen, L.; Qinghua, P.; Qi, L. Flow Pattern Identification and Pressure Drop Prediction of Oil-Water Two-Phase Flow in Horizontal Pipes. *Oil-Gas. Field Environ. Prot.* **2014**, *24*, 12–15.
9. Chang, D.; Xue, T.; Zhang, Y. Hierarchical Fuzzy Recognition of Gas-Liquid Two-Phase Flow Patterns Based on High-Speed Photography Sensor. *Transducer Microsyst. Technol.* **2016**, *35*, 58–60.
10. Liu, Y.; Luo, C.; Liu, T.; Ren, G.; Wang, Z. Prediction of Gas-Liquid Two-Phase Flow Patterns in Horizontal Gas Wells. *J. Southwest Pet. Univ. (Nat. Sci. Ed.)* **2019**, *41*, 107–112.
11. Qiu, X. Numerical Simulation Study on Transient Flow Characteristics of Liquid-Loaded Gas Wells Based on FLUENT. Master's Thesis, Southwest Petroleum University, Chengdu, China, 2021.
12. Kai, J. Experimental Study on Flow Characteristics of Foam Flow in Gas Gathering Pipes and Research on Pressure Drop Model. Master's Thesis, Xi'an Shiyou University, Xi'an, China, 2022.
13. Duns, H.; Ros, N.C.J. Vertical Flow of Gas and Liquid Mixtures in Wells. In Proceedings of the 6th World Petroleum Congress, Frankfurt am Main, Germany, 19–26 June 1963; pp. 451–465.
14. Hagedorn, A.R.; Brown, K.E. Experimental study of pressure gradients occurring during continuous two phase flow in small-diameter vertical conduits. *J. Pet. Technol.* **1965**, *17*, 475–484. [CrossRef]
15. Orkiszewski, J. Prediction two-phase pressure drops in vertical pipe. *J. Pet. Technol.* **1967**, *19*, 829–838. [CrossRef]
16. Sanchez, M.J. Comparison of Correlations for Predicting Pressure Losses in Vertical Multiphase Annular flow. Master's Thesis, The University of Tulsa, Tulsa, OK, USA, 1972.
17. Ansari, A.M.; Sylvester, N.D.; Sarica, C.; Shoham, O.; Brill, J.P. A comprehensive mechanistic model for upward two-phase flow in wellbores. *SPE Prod. Facil.* **1994**, *9*, 143–151. [CrossRef]
18. Liao, K.; Li, Y.; Yang, Z.; Zhong, H. Study on Dynamic Law of Gas-Liquid Two-Phase Pipe Flow in Water-Producing Gas Reservoirs. *Acta Pet. Sin.* **2009**, *30*, 607–612.
19. Qian, Y.; Tian, X.; He, G.; Lin, X. Optimization of Multiphase Pipe Flow Models Based on PIPSIM Software. *West-China Explor. Eng.* **2013**, *25*, 38–40, 45.
20. Zhang, Z.; Xiang, S.; Feng, X.; Liu, H.; Meng, W.; Li, Y.; Ma, C. Annulus Pressure Prediction Model for Unsteady-State Testing of Deepwater Oil and Gas Wells. *Nat. Gas. Ind.* **2020**, *40*, 80–87.
21. Xiong, Z.; Zhang, Y.; Zhang, L.; Shang, J. Numerical Simulation of Gas-Liquid Two-Phase Flow in Coalbed Methane Wellbores. *J. China Univ. Pet. (Nat. Sci. Ed.)* **2023**, *47*, 153–159.
22. Liu, Z.; Liao, R.; Luo, W.; Ribeiro, J.X.F.; Su, Y. Friction Pressure Drop Model of Gas-Liquid Two-Phase Flow in an Inclined Pipe with High Gas and Liquid Velocities. *AIP Adv.* **2019**, *9*, 085025. [CrossRef]
23. Hirt, C.W.; Nichols, B.D. Volume of Fluid (VOF) Method for the Dynamics of Free Boundaries. *J. Comput. Phys.* **1981**, *39*, 201–225. [CrossRef]
24. ANSYS Inc. *ANSYS Fluent Theory Guide*; ANSYS Inc.: Canonsburg, PA, USA, 2023.
25. Yakhot, V.; Orszag, S.A. Renormalization Group Analysis of Turbulence. I. Basic Theory. *J. Sci. Comput.* **1986**, *1*, 3–51. [CrossRef]
26. Menter, F.R. Two-Equation Eddy-Viscosity Turbulence Models for Engineering Applications. *AIAA J.* **1994**, *32*, 1598–1605. [CrossRef]

Disclaimer/Publisher's Note: The statements, opinions and data contained in all publications are solely those of the individual author(s) and contributor(s) and not of MDPI and/or the editor(s). MDPI and/or the editor(s) disclaim responsibility for any injury to people or property resulting from any ideas, methods, instructions or products referred to in the content.